

Supplemental Material

Forming and preserving aragonite in shear zones: first report of blueschist facies metamorphism in the Jabal Akhdar Dome, Oman Mountains

Zuccari C.^{1*}, Vignaroli G.¹, Callegari I.², Nestola F.³, Novella D.³, Giuntoli F.¹, Guillong M.⁴ and Viola G.^{1*}

¹ *Alma Mater Studiorum, University of Bologna, Department of Biological, Geological and Environmental Sciences - BiGeA, Bologna, Italy.*

² *German University of Technology in Oman – GUTech, Department of Applied Geosciences, Muscat, Oman*

³ *University of Padua, Department of Geosciences, Padova, Italy.*

⁴ *Department of Earth Sciences, Institute of Geochemistry and Petrology, ETH Zürich, Zurich, Switzerland.*

*Corresponding authors:

Costantino Zuccari, costantino.zuccari2@unibo.it

Giulio Viola, giulio.viola3@unibo.it

Department of Biological, Geological and Environmental Sciences
Alma Mater Studiorum – University of Bologna
Via Zamboni, 67 – 40126 Bologna (Italy)

1. Analytical details

1.1 U-Pb LA-ICP-MS Analysis

Calcite U-Pb dating was performed by laser ablation inductively coupled plasma mass spectrometry (LA-ICP-MS) on polished thick sections. The analyses were conducted at the ETH Zürich, Switzerland, by using a RESOLUTION laser ablation system with a 193 nm excimer (ArF) laser source and a two-volume Laurin Technic S-155 ablation cell coupled to a Thermo Element XR sector-field ICP-MS equipped with a high-capacity interface pump. The analytical and data reduction protocols follow Roberts et al. (2017) using NIST 614 and WC-1 primary reference materials and Guillong et al. (2020) using spot sizes of 110 and 163 μm with a matched ablation crater aspect ratio for the reference materials and unknowns. U-Pb ages were calculated from Tera-Wasserburg concordia lower intercepts using the IsoplotR software package (Vermeesch, 2018). All uncertainties are reported at the 95% confidence level. A long-term excess variance of 2% relative was propagated

by quadratic addition to the uncertainty of the individual lower intercept dates (Guillong et al., 2020). In addition to the samples, the two secondary reference materials ASH15D (Nuriel et al., 2021) and JT (Guillong et al., 2020) were analyzed in all sessions for validation. Correction for matrix effects with WC-1 was done with anchoring to 0.85 common-lead while samples and secondary reference materials were not anchored. No disequilibrium correction was applied.

1.2 Raman spectroscopy on carbonaceous material

Micro-Raman spectra on graphite (Fig. 3A) were obtained using a ThermoScientific DXR Raman microscope installed at the Department of Chemistry Sciences, University of Padova, Italy. We used a 50× objective and a 532 nm excitation source. Laser power was 1 mW (to avoid graphite damage) and Raman spectra were collected for about 900 s. The spatial resolution was about 1.1 μm, whereas the spectral resolution was about 2.5 cm⁻¹.

The Omnic software (Thermo Fisher Scientific) was used for Raman spectrum decomposition by using the software Lorentian/Gaussian function, following the procedure described in Kouketsu et al. (2014). Peaks with centre in position at ~1580 cm⁻¹, 1350 cm⁻¹ and 1620 cm⁻¹ were identified respectively as G, D1 and D2. The R2 parameter, defined as the ratio between the peaks area D1/(D1+D2+G), was calculated for each measurement.

A linear relationship between temperature and the Raman parameter R2 forms the basis of the CM geothermometer (Beysac et al., 2002). The temperature can be estimated to ± 50° C in the range 330–650° C. Deformation can affect the internal disorder and underestimate the temperature obtained from the spectra analysis (Kirilova et al., 2018). Care was thus taken to avoid measuring CM within cracks, and to prevent altered measurement from CM damaged during the thin section polishing; we performed measurements by focusing the laser beam on CM beneath the surface of a transparent adjacent grain as suggested in Beysac et al. (2002). CM in the host rock was analysed with λ=473 nm, while CM in the mylonite was analysed with λ=532 nm. To avoid errors in the temperature estimation we applied two different geothermometers calibrated for the different laser wavelength used to collect the data: Beysac et al. (2002) for the λ=475 nm analysis and Aoya et al. (2010) for the λ=532 nm analysis. Although both yield similar results, the equation given in Beysac et al. (2002) for the Raman CM geothermometer is linear whereas that in Aoya et al. (2010) is quadratic.

1.3 High-resolution Micro-Raman Spectroscopy maps

High-resolution micro-Raman spectra of calcite-aragonite crystals and fibres were produced with a Witec Alpha 300 R Raman microscope installed at the Department of Geosciences, University of Padova, Italy. In particular, 2D maps were collected on samples CZ2004B and CZ2018 by using a 50X objective and a 532 nm excitation wavelength. At the conditions employed during the analyses, the spectral resolution was $\sim 3 \mu\text{m}$ while the spatial resolution is $< 1 \mu\text{m}$.

The analyses employed a nominal laser power of 40 mW and integration time of 0.5 s. The high power and low integration time were selected to collect a large number of spectra in a reduced amount of time, while maintaining a high intensity of the signal. In fact, the maps for samples CZ2004B and CZ2004B covered a 300×300 and $400 \times 400 \mu\text{m}^2$ area, respectively, where single spot analyses were collected at $1 \mu\text{m}$ steps.

CAPTIONS TO FIGURES AND TABLES

Fig. S1. Microphotograph of the protolith undeformed Hajir Fm outside of the mylonitic shear zones. A) Plain polarized view of the Hajir Fm organic matter-rich carbonate containing abundant dispersed graphite. B) Crossed polarized view of (A) highlighting twinned calcite grains. C) Plain polarized view microphotograph of the typical mylonitic fabric. The mylonitic foliation is outlined by highly transposed and aligned relic carbonate grains. Samples used for RSCM are from these mylonitic shear zones, where graphite-rich layers outline and define the foliation. D-E) Plain polarized and crossed polarized view of twinned calcite porphyroclast mantled by recrystallised new grains.

Fig. S2. Microphotographic evidence of brittle – ductile deformation cyclicity. A-B) Plain and crossed polarized view of calcmylonitic fabric cut across by mode-I veins infilled by stretched aragonite and quartz fibres. Fibres do not exhibit evidence of plastic deformation. C-D) Plain and crossed polarized view of stretched, segmented and transposed veins and fibres composed of quartz and aragonite-calcite. Veins and fibres, related to an earlier transient brittle phase, are transposed within and along the mylonitic foliation of the calcmylonitic shear zones.

Fig. S3. Cathodoluminescence imaging of brittle and ductile fabrics. A-B) Cross polarized and cathodoluminescence images of detail in Fig. S2A-B, where stretched vein of quartz is represented by the dark brown/black. C-D) Cross polarized and cathodoluminescence images of Fig. 2C, showing the difference in chromatic response of rod-shaped aragonite grains (dark orange) and of multiple late fractures (bright orange). E-F) Cross polarized and cathodoluminescence images of structural relationships of rod-shaped aragonite grains with strong SPO (dark orange) and late veins cutting across and along the main foliation (bright orange). G-H) Cross polarized and cathodoluminescence images showing the constant dark brown sign of rod-shaped aragonite grains. Note that no evidence of reaction between fluids infilling fractures and the calcmylonitic fabric is present.

Fig. S4. Location of points for trace element analysis within quartz and aragonite veins filling mode-I fracture within the mylonitic shear zone. Refer to Table S1 for numerical data. Is not possible to discriminate which phase is investigated (aragonite or calcite) due to the size difference between LA-ICP-MS spot (hundreds of microns) and preserved aragonite (2 to ~ 20 micron²).

Fig. S5. Trace element pattern of aragonite and calcite pseudomorphs over aragonite reported in Table S1. Spot location is shown in Fig. S4. Points from the rod-shaped crystals of the mylonitic shear zone are reported in the grey field.

Fig S6. U-Pb radiometric constraints and overview of spot points. A) Hand specimen of calcmylonite. Spots analysed for dating are shown. B) Example of dated elongated fibres. C) Example of dated mode-I fibres. D) Example of dated rod-shaped grains. E) U-Pb Tera-Wasserburg (Tera and Wasserburg, 1972) plot of calcite-aragonite fibres. F) U-Pb Tera-Wasserburg plot of calcite-aragonite crystals of mylonitic fabric, yielding Upper Cretaceous (above) and upper Ediacaran (bottom) ages. G) Summary plot of existing radiometric constraints on the principal tectonic events dated for the Jabal Akhdar and Saih Hatat Domes (data from Garber et al., 2021; Gray et al., 2004; Grobe et al., 2019; Lippard, 1983; Ninkabou et al., 2021; Tavani et al., 2020; Warren et al., 2003). For all Tera-Wasserburg plots, the grey area is 2 σ error envelopes of the regression line.

Table S1. Trace elements within aragonite and calcite pseudomorphs over aragonite crystals and fibres. Analysed spots are shown in Fig. S4.

References

- Aoya, M., Kouketsu, Y., Endo, S., Shimizu, H., Mizukami, T., Nakamura, D., and Wallis, S., 2010, Extending the applicability of the Raman carbonaceous-material geothermometer using data from contact metamorphic rocks: *Journal of Metamorphic Geology*, v. 28, p. 895–914, doi:10.1111/j.1525-1314.2010.00896.x.
- Beyssac, O., Goffé, B., Chopin, C., and Rouzaud, J.N., 2002, Raman spectra of carbonaceous material in metasediments: A new geothermometer: *Journal of Metamorphic Geology*, v. 20, p. 859–871, doi:10.1046/j.1525-1314.2002.00408.x.
- Garber, J.M., Rioux, M., Searle, M.P., Kylander-Clark, A.R.C., Hacker, B.R., Vervoort, J.D., Warren, C.J., and Smye, A.J., 2021, Dating Continental Subduction Beneath the Samail Ophiolite: Garnet, Zircon, and Rutile Petrochronology of the As Sifah Eclogites, NE Oman: *Journal of Geophysical Research: Solid Earth*, v. 126, p. e2021JB022715, doi:10.1029/2021JB022715.

- Gray, D.R., Miller, J.M.L., Foster, D.A., and Gregory, R.T., 2004, Transition from subduction- to exhumation-related fabrics in glaucophane-bearing eclogites, Oman: Evidence from relative fabric chronology and $^{40}\text{Ar}/^{39}\text{Ar}$ ages: *Tectonophysics*, v. 389, p. 35–64, doi:10.1016/j.tecto.2004.06.016.
- Grobe, A., von Hagke, C., Littke, R., Dunkl, I., Wübbeler, F., Muchez, P., and Urai, J.L., 2019, Tectono-Thermal evolution of Oman's Mesozoic passive continental margin under the obducting Semail Ophiolite: A case study of Jebel Akhdar, Oman: *Solid Earth*, v. 10, p. 149–175, doi:10.5194/se-10-149-2019.
- Guillong, M., Wotzlaw, J.-F., Looser, N., and Laurent, O., 2020, Evaluating the reliability of U–Pb laser ablation inductively coupled plasma mass spectrometry (LA-ICP-MS) carbonate geochronology: matrix issues and a potential calcite validation reference material: *Geochronology*, v. 2, p. 155–167, doi:10.5194/gchron-2-155-2020.
- Kirilova, M., Toy, V., Rooney, J.S., Giorgetti, C., Gordon, K.C., Collettini, C., and Takeshita, T., 2018, Structural disorder of graphite and implications for graphite thermometry: *Solid Earth*, v. 9, p. 223–231, doi:10.5194/se-9-223-2018.
- Kouketsu, Y., Mizukami, T., Mori, H., Endo, S., Aoya, M., Hara, H., Nakamura, D., and Wallis, S., 2014, A new approach to develop the $^{37}\text{Rb}/^{87}\text{Rb}$ aman carbonaceous material geothermometer for low-grade metamorphism using peak width: *Island Arc*, v. 23, p. 33–50, doi:10.1111/iar.12057.
- Lippard, S.J., 1983, Cretaceous high pressure metamorphism in NE Oman and its relationship to subducted and ophiolite nappe emplacement.: *Journal of the Geological Society*, v. 140, p. 97–104, doi:10.1144/GSJGS.140.1.0097.
- Ninkabou, D., Agard, P., Nielsen, C., Smit, J., Gorini, C., Rodriguez, M., Haq, B., Chamot-Rooke, N., Weidle, C., and Ducassou, C., 2021, Structure of the Offshore Obducted Oman Margin: Emplacement of Semail Ophiolite and Role of Tectonic Inheritance: *Journal of Geophysical Research: Solid Earth*, v. 126, p. 1–28, doi:10.1029/2020JB020187.
- Nuriel, P., Wotzlaw, J.-F., Ovtcharova, M., Vaks, A., Stremtan, C., Šala, M., Roberts, N.M.W., and Kylander-Clark, A.R.C., 2021, The use of ASH-15 flowstone as a matrix-matched reference material for laser-ablation U – Pb geochronology of calcite: *Geochronology*, v. 3, p. 35–47, doi:10.5194/gchron-3-35-2021.
- Roberts, N.M.W., Rasbury, E.T., Parrish, R.R., Smith, C.J., Horstwood, M.S.A., and Condon, D.J., 2017, A calcite reference material for LA-ICP-MS U-Pb geochronology: *Geochemistry, Geophysics, Geosystems*, v. 18, p. 2807–2814, doi:10.1002/2016GC006784.
- Tavani, S., Corradetti, A., Sabbatino, M., Seers, T., and Mazzoli, S., 2020, Geological record of the transition from induced to self-sustained subduction in the Oman Mountains: *Journal of Geodynamics*, v. 133, p. 101674, doi:10.1016/j.jog.2019.101674.

- Tera, F., and Wasserburg, G.J., 1972, U-Th-Pb systematics in three Apollo 14 basalts and the problem of initial Pb in lunar rocks: *Earth and Planetary Science Letters*, v. 14, p. 281–304, doi:10.1016/0012-821X(72)90128-8.
- Vermeesch, P., 2018, IsoplotR: A free and open toolbox for geochronology: *Geoscience Frontiers*, v. 9, p. 1479–1493, doi:10.1016/J.GSF.2018.04.001.
- Warren, C.J., Parrish, R.R., Searle, M.P., and Waters, D.J., 2003, Dating the subduction of the Arabian continental margin beneath the Semail ophiolite, Oman: *Geology*, v. 31, p. 889–892, doi:10.1130/G19666.1.

Table S1. Trace elements within aragonite and calcite pseudomorphs over aragonite crystals and fibres. Analysed spots are shown in Fig. S4.

Sample and point number	Mg25 ppm mean	Mg wt %	Mn55 ppm mean	Mn wt %	Fe57 ppm mean	Fe wt %	Sr88 ppm mean	Sr wt %	Pb208 ppm mean	Pb208 wt %	Th232 ppm mean	Th232 wt %	U238 ppm mean	U238 wt %	Fabric
CZ2004B - 1	2,111	0.2111	778	0.078	484	0.048	1,255	0.1255	183.00	0.0183	0.12	0.00001	0.686	0.0001	Mode-I fibres
CZ2004B - 2	117,104	11.7104	358	0.036	35	0.004	1,137	0.1137	1.33	0.0001	0.02	0.00000	0.248	0.0000	
CZ2004B - 3	2,678	0.2678	561	0.056	279	0.028	1,986	0.1986	31.18	0.0031	0.07	0.00001	0.270	0.0000	
CZ2004B - 4	2,905	0.2905	255	0.025	41	0.004	2,195	0.2195	3.71	0.0004	0.08	0.00001	0.102	0.0000	
CZ2004B - 5	2,788	0.2788	337	0.034	35	0.003	1,755	0.1755	5.12	0.0005	0.09	0.00001	0.108	0.0000	
CZ2004B - 6	3,432	0.3432	374	0.037	88	0.009	2,627	0.2627	13.34	0.0013	0.07	0.00001	0.128	0.0000	
CZ2004B - 7	2,064	0.2064	757	0.076	424	0.042	1,233	0.1233	87.50	0.0087	0.08	0.00001	0.837	0.0001	
CZ2004B - 9	3,665	0.3665	355	0.036	1,520	0.152	1,826	0.1826	41.77	0.0042	4.05	0.00041	6.079	0.0006	
CZ2004B - 10	40,626	4.0626	704	0.070	42,972	4.297	1,162	0.1162	115.29	0.0115	7.92	0.00079	9.235	0.0009	
CZ2004B - 11	2,732	0.2732	313	0.031	881	0.088	1,974	0.1974	33.96	0.0034	1.48	0.00015	2.109	0.0002	
CZ2004B - 12	1,948	0.1948	832	0.083	492	0.049	1,148	0.1148	92.37	0.0092	0.15	0.00002	1.106	0.0001	Mode-I fibres
CZ2004B - 13	3,405	0.3405	367	0.037	59	0.006	1,913	0.1913	13.34	0.0013	0.09	0.00001	0.662	0.0001	
CZ2004B - 14	2,101	0.2101	977	0.098	492	0.049	1,284	0.1284	182.37	0.0182	0.03	0.00000	1.135	0.0001	
CZ2004B - 16	3,258	0.3258	348	0.035	81	0.008	2,432	0.2432	18.19	0.0018	0.08	0.00001	0.137	0.0000	
CZ2004B - 17	1,674	0.1674	204	0.020	32	0.003	989	0.0989	0.12	0.0000	0.02	0.00000	0.019	0.0000	
mean in wt %		1.2833		0.05		0.319		0.16610		0.0055		0.0001		0.0002	

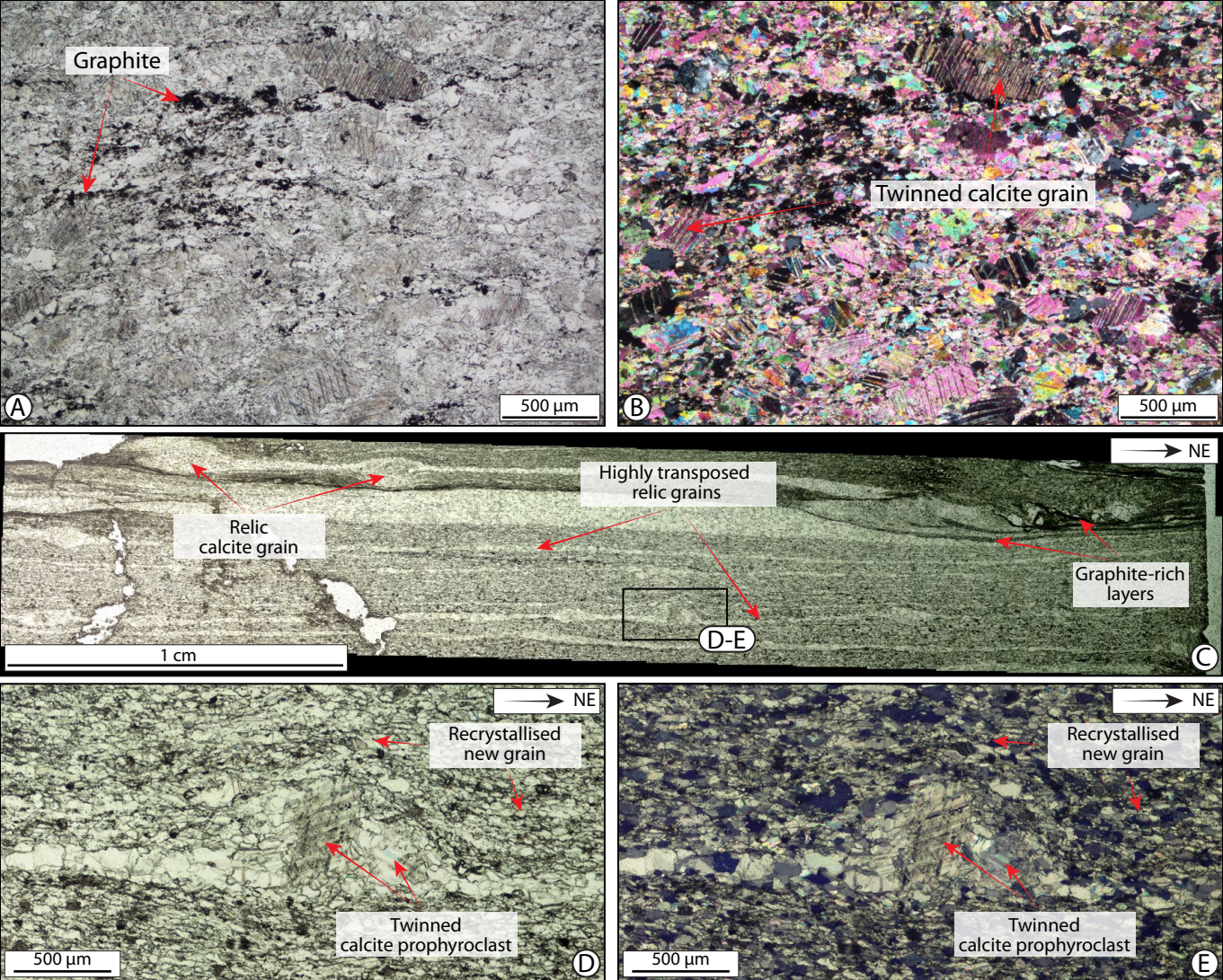


Fig. S1

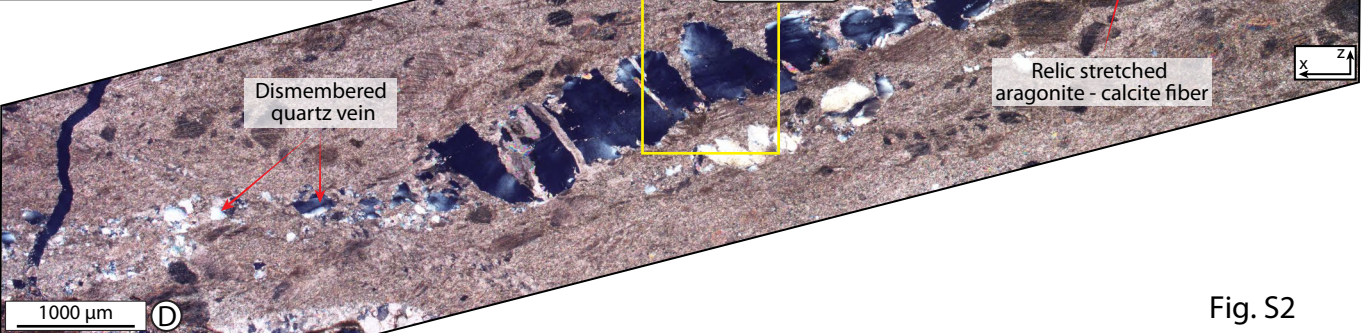
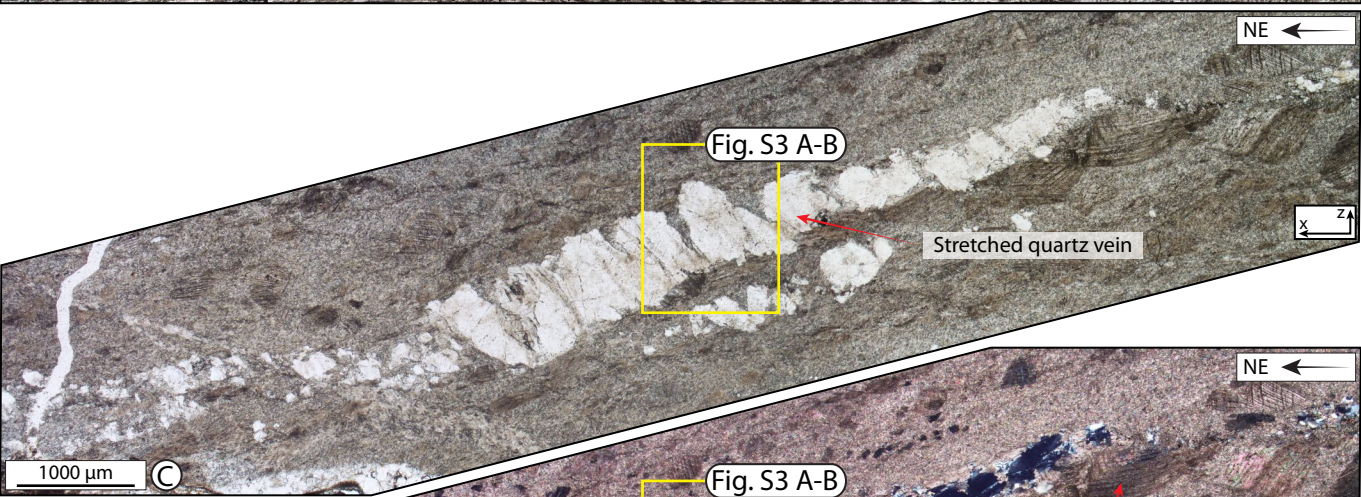
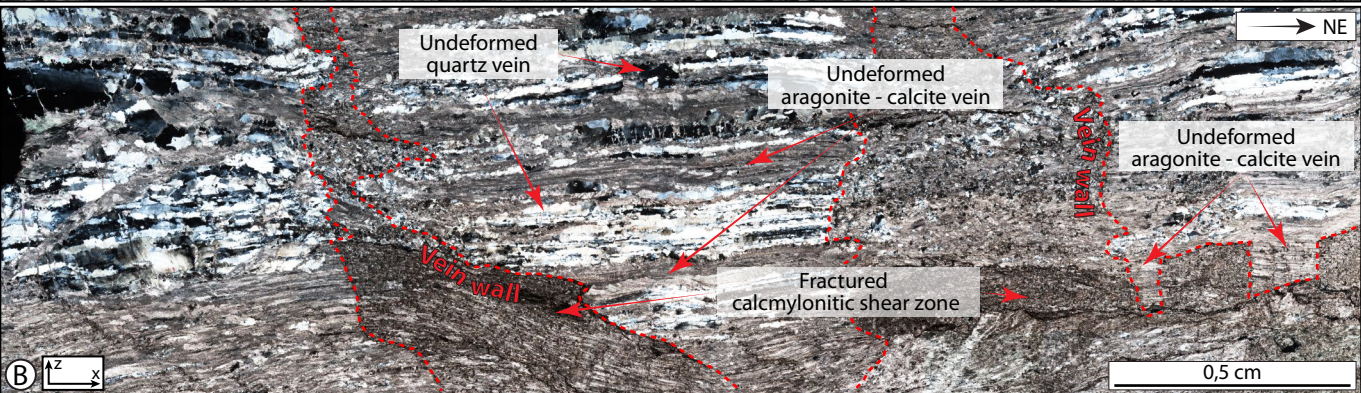
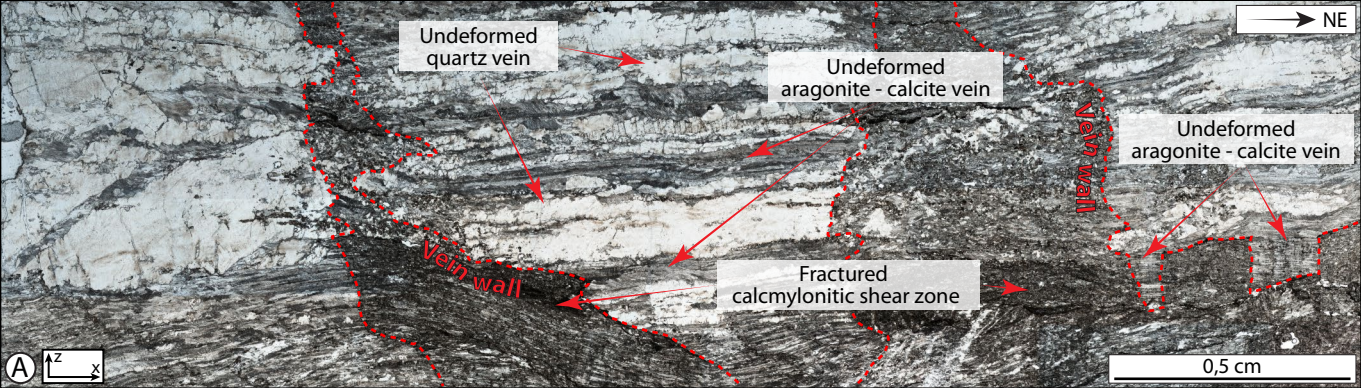


Fig. S2

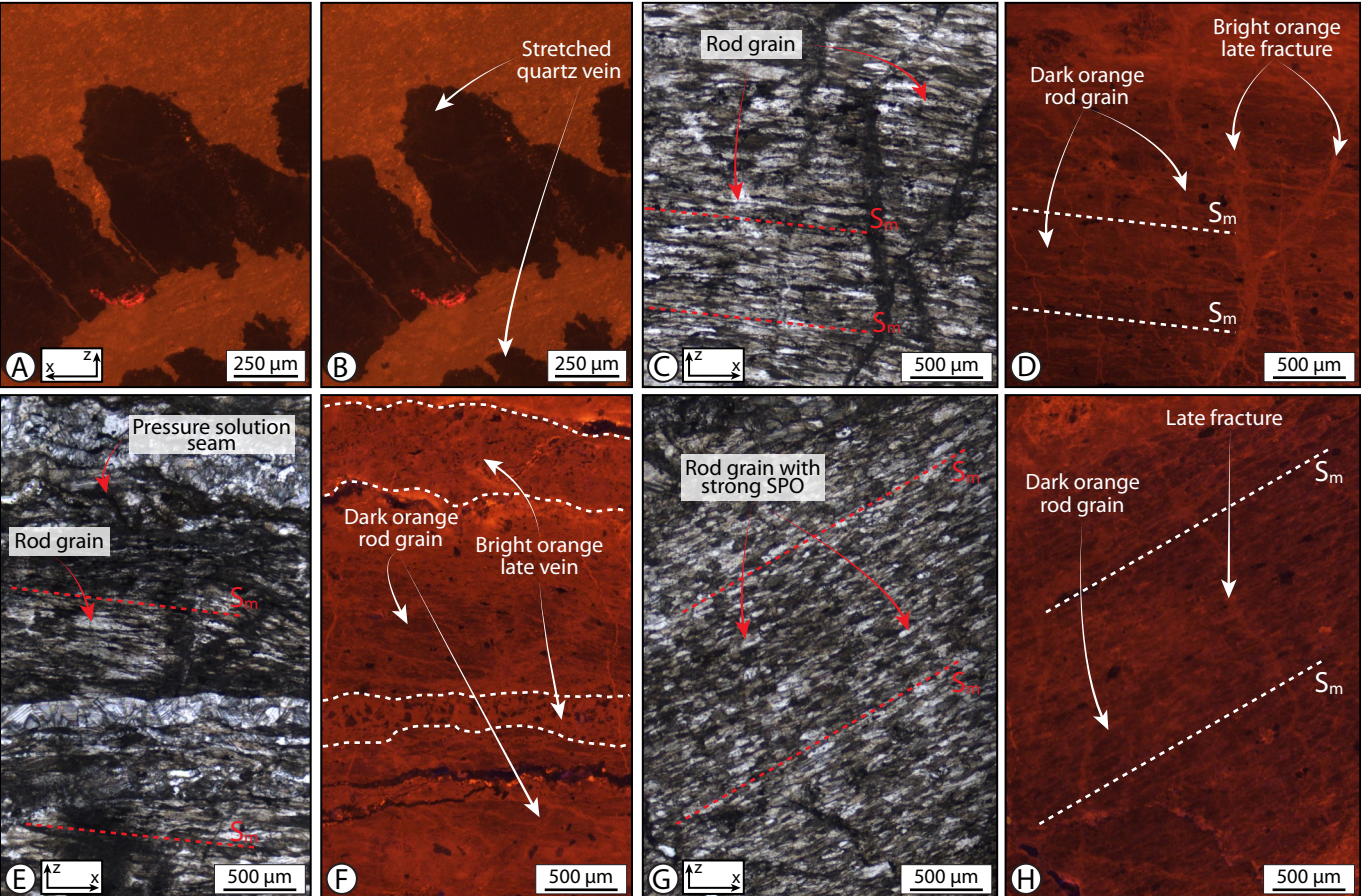


Fig. S3

Fig. S4

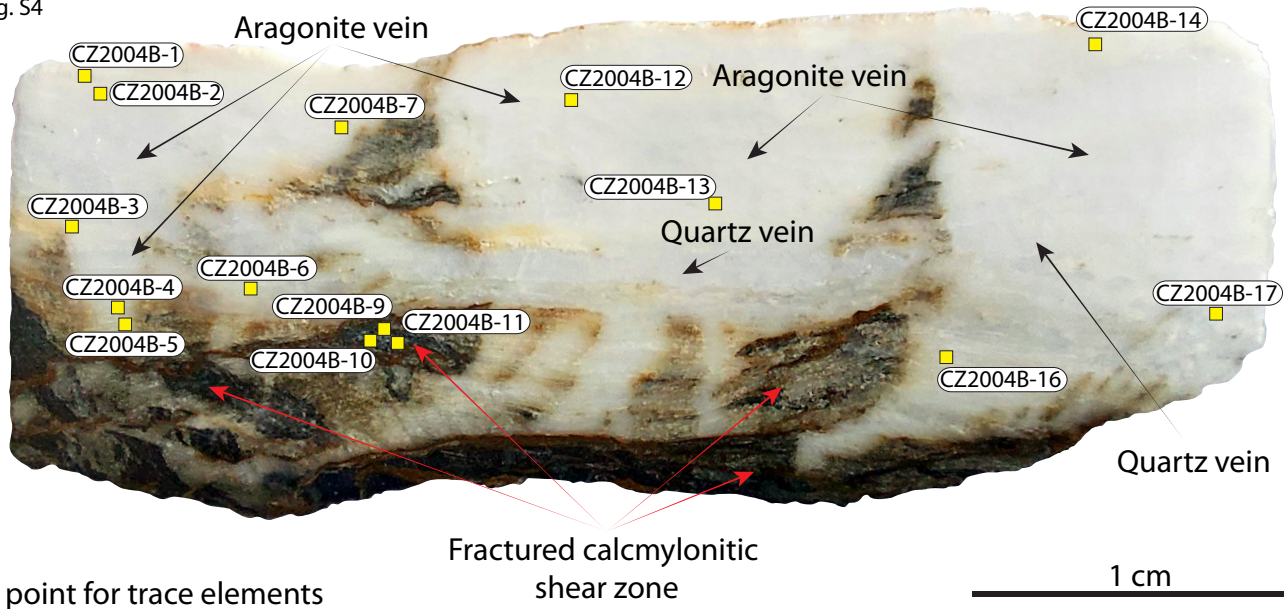
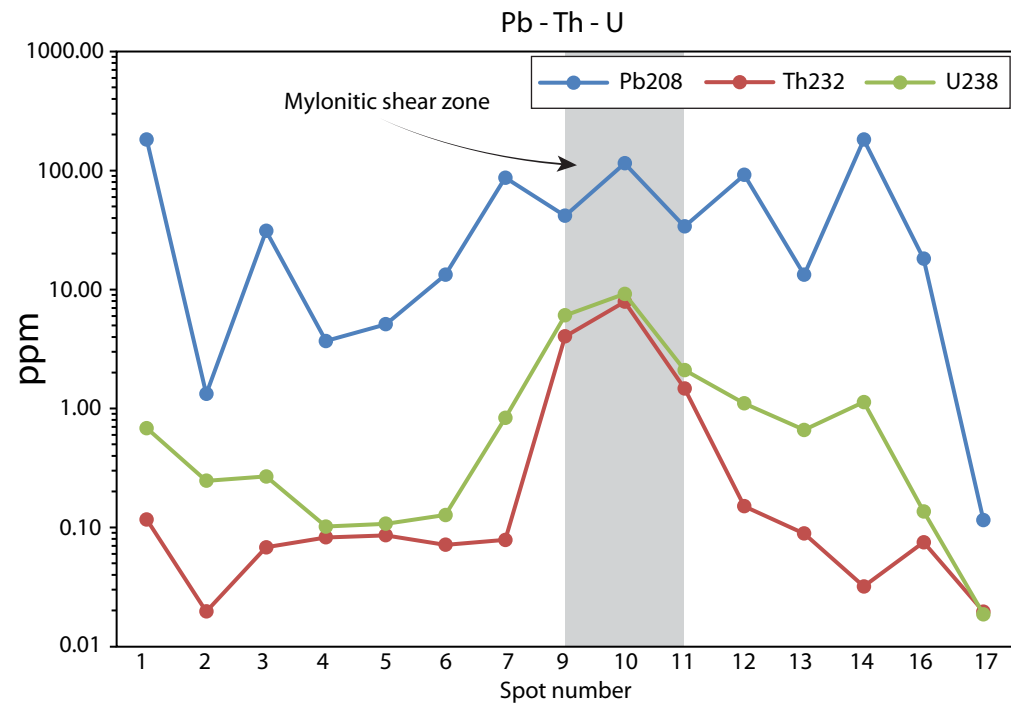
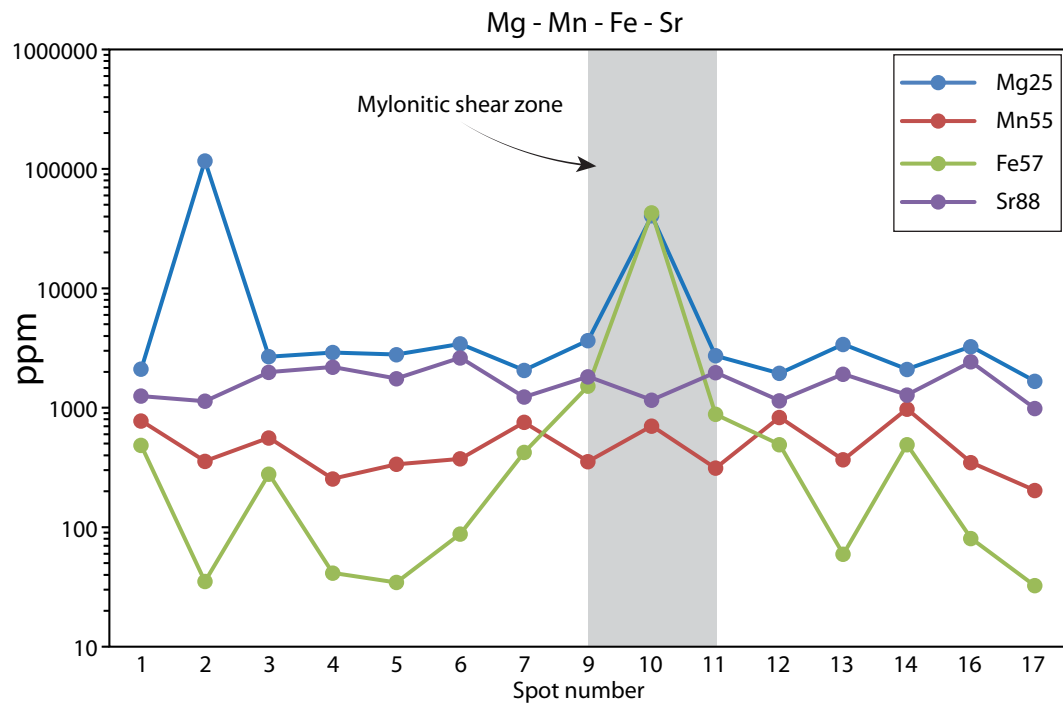


Fig. S5



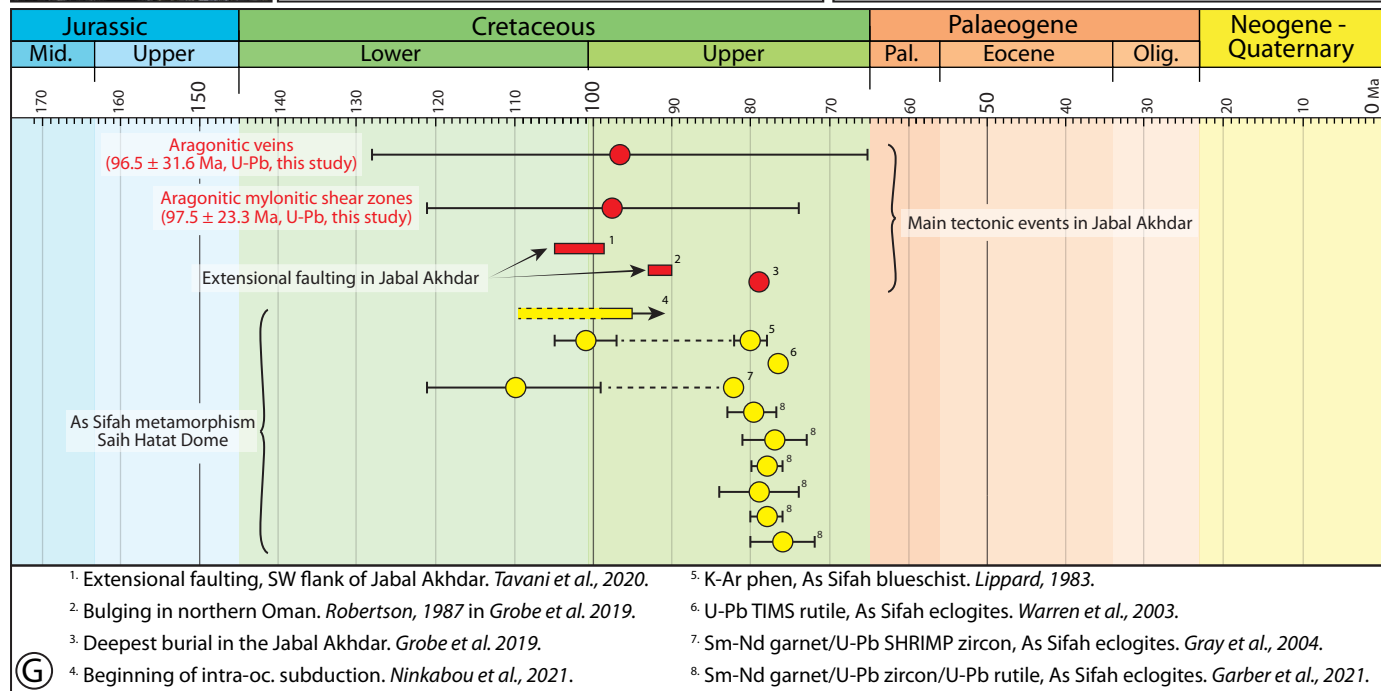
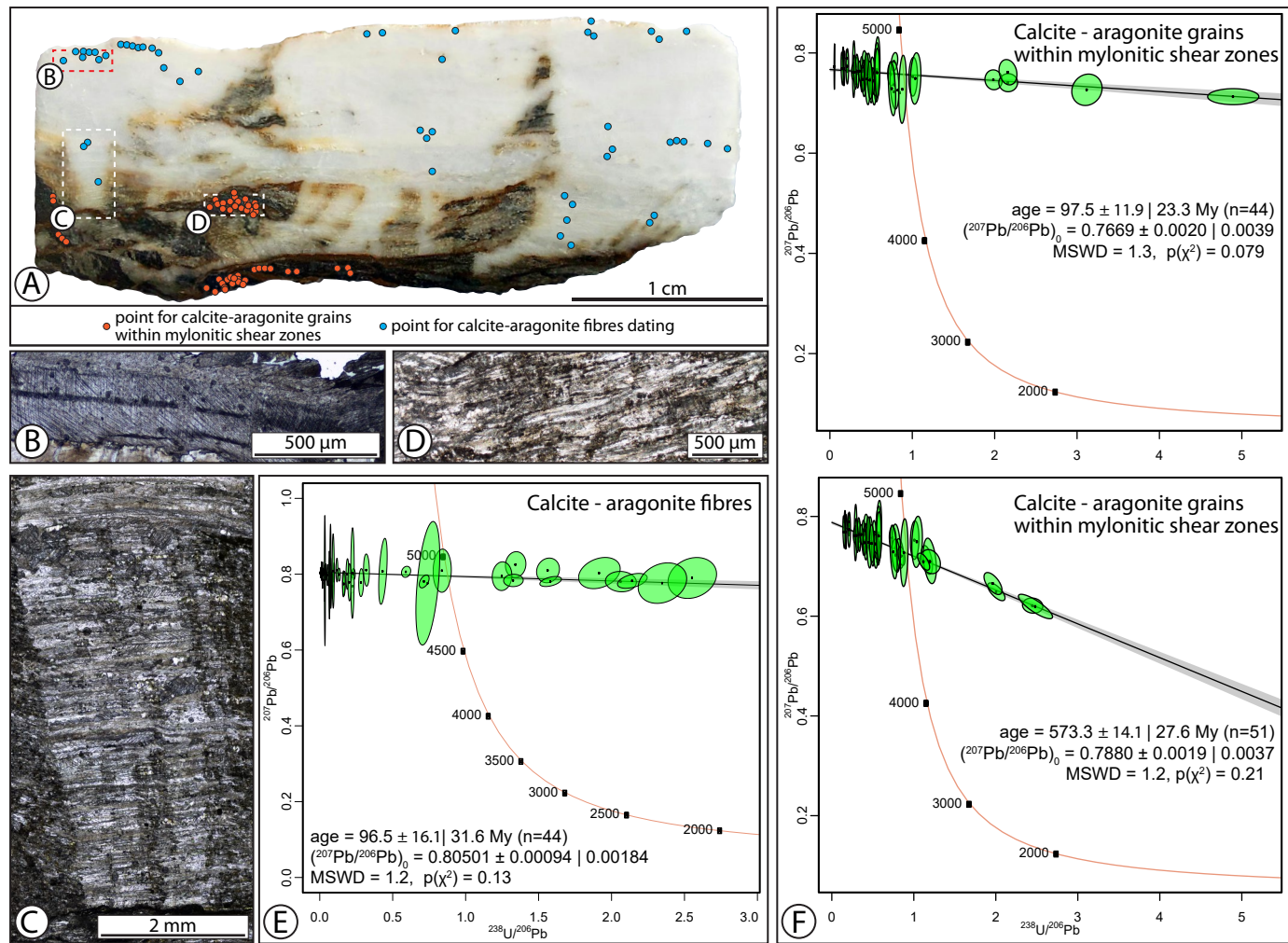


Fig. S6